

# Strong Quantum Coupling in the Vibrational Signatures of a Symmetric Ionic Hydrogen Bond: The Case of $(\text{CH}_3\text{OH})_2\text{H}^+$

Jake A. Tan<sup>†,‡,§</sup> and Jer-Lai Kuo<sup>\*,†,§</sup>

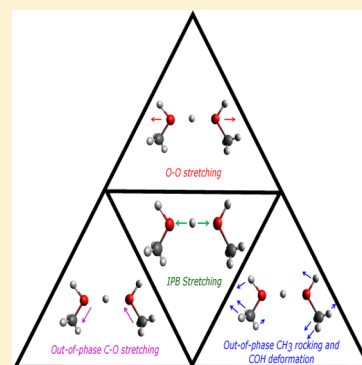
<sup>†</sup>Molecular Science and Technology Program, Taiwan International Graduate Program, Academia Sinica, 128 Academia Road, Section 2, Nangang, Taipei 115, Taiwan, ROC

<sup>‡</sup>Department of Chemistry, National Tsing Hua University, 101 Kuang-Fu Road, Section 2, Hsinchu 30013, Taiwan, ROC

<sup>§</sup>Institute of Atomic and Molecular Sciences, Academia Sinica, No.1 Roosevelt Road, Section 4, Taipei 10617, Taiwan, ROC

## S Supporting Information

**ABSTRACT:** Vibrational coupling between proton and flanking group motions in the ionic hydrogen bond (IHB) of  $(\text{CH}_3\text{OH})_2\text{H}^+$  were studied by solving reduced-dimension vibrational Schrödinger equations. Potential energy and dipole surfaces along a few key normal modes were constructed with high-level *ab initio* methods. It was found that the IHB stretch parallel to O–O axis strongly couples with the out-of-phase C–O stretch and out-of-phase in-plane  $\text{CH}_3$  rock with COH deformation. Such strong quantum coupling leads to a complex triplet at  $850\text{--}1100\text{ cm}^{-1}$  region. Furthermore, we have investigated the possible active role of torsional motion in intensity redistribution.



## 1. INTRODUCTION

The existence of the ionic hydrogen bond (IHB) is one of the most fascinating themes in nature. Chemically, it plays a key role in the transport of the most ubiquitous ion in aqueous media.<sup>1</sup> Biologically, it is found in photosynthetic processes and enzymatic catalysis as well as proton pumps between two sides of a cell membrane.<sup>2,3</sup> In a structural perspective, an IHB refers to an excess proton ( $\text{H}^+$ ) under a tug-of-war between the electronegative atoms of two closed-shell molecules.<sup>4,5</sup> Examples of IHB include proton-bridged dimers:  $\text{F}^-\cdots\text{H}^+\cdots\text{F}^-$ ,  $\text{H}_2\text{O}\cdots\text{H}^+\cdots\text{OH}_2$ ,  $\text{H}_3\text{N}\cdots\text{H}^+\cdots\text{OH}_2$ , and  $(\text{CH}_3)_3\text{N}\cdots\text{H}^+\cdots\text{NH}_3$ . In such structures, the bond between the electronegative atom and  $\text{H}^+$  are longer than usual, an indication that  $\text{H}^+$  is shared between the two electronegative atoms and hence classifying them under the family of Zundel-type structures. Such IHB motifs ( $\text{O}-\text{H}^+-\text{O}$ ,  $\text{N}-\text{H}^+-\text{O}$ , and  $\text{N}-\text{H}^+-\text{N}$ ) are of particular interest in the controversial role of low-barrier hydrogen bonds (LBHB) in metabolic processes.<sup>6</sup> Specific examples of LBHB's include proton-coupled bicarboxylates, which are believed to stabilize high-energy reaction intermediates in HIV-1 protease.<sup>6</sup> Another case would be the hydrogen bond between the imidazole side chain of His-95 and the enediolate intermediate of triosephosphate isomerase, an atom economy enhancing step in glycolysis.<sup>6</sup>

Over the last few decades, sophisticated experimental techniques such as infrared multiphoton dissociation (IRMPD) and “messenger atom” action spectroscopy have been used to study proton bound dimers in the gas phase.<sup>4,5,7–16</sup> Both of these methods were developed in Lee's

group<sup>17,18</sup> in the late 80s. Among the two techniques, the “messenger atom” technique typically provides narrower and sharper bands due to the cooling effect of the messenger atom.<sup>12</sup> Furthermore, the weaker binding of the messenger atom permits dissociation to occur at lower photon energy, extending the range of accessible vibrational frequencies.

The most extensively studied Zundel IHB is  $\text{H}_5\text{O}_2^+$ , where both “messenger atom” action spectroscopy<sup>5,12,14,17,19</sup> and IRMPD<sup>7,10,15,17</sup> spectra, as well as theoretical<sup>1,14,19–33</sup> treatments, can be found in the literature. There is a general consensus<sup>21,22,28</sup> that the IHB fundamental stretch parallel to the heavy atom (O–O) axis is located around  $1000\text{ cm}^{-1}$ . In neon-tagged proton bound water dimer,  $\text{Ne}\cdot\text{H}_5\text{O}_2^+$ , the most noticeable spectral feature is the strong doublet around  $1000\text{ cm}^{-1}$ . Recovering the doublet in theoretical treatments was found to be difficult<sup>4,21</sup> that it took a full 15-dimensional calculations by Vendrell and co-workers<sup>24–27</sup> to explain its origin. Their calculation was aided by the efforts of Bowman and co-workers<sup>29</sup> in constructing the 15-dimensional potential and dipole surfaces at CCSD(T)/aug-cc-pVTZ level. Currently, it is established that the said doublet is caused by the strong coupling between IHB stretching parallel to O–O axis and a combination band involving O–O stretching, and water wagging mode.<sup>25,30</sup>

Given the fact that  $\text{H}_5\text{O}_2^+$  has been widely understood, it would be worthwhile to examine the next member of the

Received: October 28, 2015

Published: November 2, 2015



homologous series,  $(\text{CH}_3\text{OH})_2\text{H}^+$ . Compared with  $\text{H}_2\text{O}$ ,  $\text{CH}_3\text{OH}$  has CO stretching and  $\text{CH}_3$  rocking; their frequencies are in the vicinity of  $1000\text{ cm}^{-1}$ . This in turn opens the direction of studying the interaction of IHB stretch with other fundamental bands near  $1000\text{ cm}^{-1}$ . Furthermore, Johnson<sup>4</sup> and Fridgen<sup>9</sup> previously reported their messenger-tagged and IRMPD spectra, respectively, making theoretical treatments accessible for experimental comparisons. It is interesting to mention that both the IRMPD and messenger-tagged spectra for  $(\text{CH}_3\text{OH})_2\text{H}^+$  are in reasonable agreement with each other at  $800\text{--}1050\text{ cm}^{-1}$ . By comparing the IRMPD bands with harmonic frequencies obtained at B3LYP/6-31+G\*\*, Fridgen<sup>9</sup> assigned the peaks at  $866$  and  $982\text{ cm}^{-1}$  as the IHB stretch parallel to the O–O axis and C–O stretch, respectively. However, both Johnson<sup>4</sup> and Fridgen<sup>9</sup> have speculated that flanking group motions couple with the IHB stretch, making the spectral assignment inherently difficult. In addition, the IHB stretch is highly anharmonic due to the proton's large amplitude motion. As a result, treatment beyond harmonic level is essential for further understanding of these bands.

In this article, we report our investigations on the coupling between IHB stretch parallel to O–O axis and flanking group motions using  $(\text{CH}_3\text{OH})_2\text{H}^+$  as the system. We have utilized second-order Møller–Plesset perturbation theory (MP2)<sup>34</sup> with aug-cc-pVDZ as the basis set to optimize (minimize) the structure and compute the Hessian matrix to extract normal modes. Vibrational coupling among a given set of normal modes is treated explicitly by solving a vibrational Schrödinger equation. This is achieved by the method of harmonic oscillator discrete variable representation (DVR).<sup>35–38</sup> Integrated absorption coefficients, however, are evaluated on the basis of Fermi Golden rule.<sup>39</sup> The required potential surfaces are computed using either MP2 or coupled cluster singles and doubles with noniterative triple excitations (CCSD(T)).<sup>40,41</sup> Dipole surfaces, however, are constructed from either the MP2 or CCSD level. Lastly, we performed similar calculations at the B3LYP<sup>42</sup> level for comparative purposes.

## 2. THEORETICAL METHODS

### Conformational Search via Geometry Optimization.

In real-time measurement, a spectrum obtained from both “messenger atom” technique and IRMPD are convolutions of a spectrum associated with each stable conformers. As a result, identification of the possible conformers is indispensable in understanding the experimental spectrum. Fridgen<sup>9</sup> identified two conformers for  $(\text{CH}_3\text{OH})_2\text{H}^+$  at the B3LYP 6-31+G\*\* level. A geometry optimization was performed for the singlet, ground state of  $(\text{CH}_3\text{OH})_2\text{H}^+$  at MP2/aug-cc-pVDZ using Gaussian09 suite of programs.<sup>43</sup> Furthermore, the same initial geometry was optimized at larger basis sets: 6-311++G-(3df,3pd) and aug-cc-pVTZ. It was found that there are no significant differences between the minima structures across these basis sets. In particular, differences between bond lengths, bond angles, and dihedral angles are within  $0.02\text{ Å}$ ,  $3^\circ$ , and  $6^\circ$  respectively.

From the obtained minima structure at MP2/aug-cc-pVDZ, we performed a relaxed scan along the  $\angle\text{HOOH}$  dihedral angle with the same level and basis set. Two minimum structures were identified. Following Fridgen's notation,<sup>9</sup> these conformers are labeled as MA and MB (Figure 1) with MA as the global minimum. In both conformers, the shared proton is located at the midpoint of the O–O axis, which is a strong attribute of Zundel structures.<sup>9,21,44</sup> The optimized Z-matrix

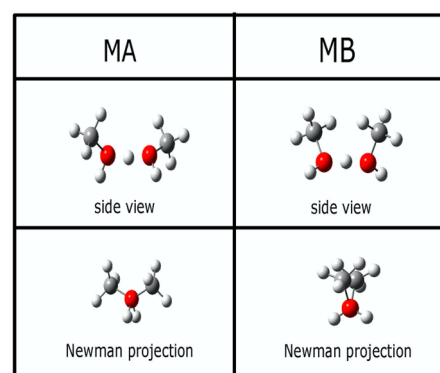


**Figure 1.** Representation of the two stable conformers of  $(\text{CH}_3\text{OH})_2\text{H}^+$  obtained at MP2/aug-cc-pVDZ. These conformers are labeled as MA and MB. The top rows are side views and the bottom rows are Newman projections. Among the two conformers, MA is more stable.

coordinates for both conformers can be found in the [Supporting Information](#) (Figures S1 and S2 and Tables S1 and S2). The potential energy curve corresponding to the dihedral scan is shown in [Figure 2](#). The relative electronic

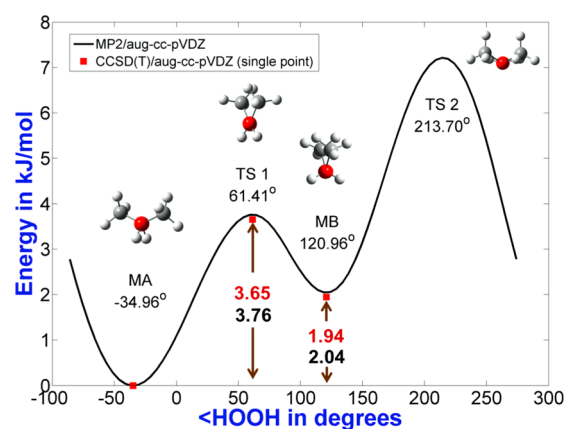


**Figure 2.** Two stable conformers of  $(\text{CH}_3\text{OH})_2\text{H}^+$  obtained via a relaxed dihedral scan at MP2/aug-cc-pVDZ. The red squares in the figure below are CCSD(T)/aug-cc-pVDZ//MP2/aug-cc-pVDZ single-point energies. Conformer MA has the lowest energy and is related to MB by a dihedral angle ( $\angle\text{HOOH}$ ) rotation. The energy difference (without ZPE correction) between MA and MB are  $2.04$  and  $1.94\text{ kJ/mol}$  for MP2/aug-cc-pvdz//MP2/aug-cc-pVDZ (black) and CCSD(T)/aug-cc-pVDZ//MP2/aug-cc-pVDZ (red), respectively. The same coloring scheme corresponds to the TS 1 barrier.

energies, zero-point energy (ZPE) corrected energies and Gibbs free energies at  $68\text{ K}$  are listed in [Table 1](#). Across all basis sets, conformer MA is consistently a global minimum. Note that the electronic and free energy difference between aug-cc-pVDZ and aug-cc-pVTZ is within  $0.2\text{ kJ/mol}$ . For this reason, we believed that aug-cc-pVDZ would be a good and economical basis set for this study.

**Possible Vibrational Modes in the  $800\text{--}1100\text{ cm}^{-1}$  Region.** Because the interest of this study is to explore the intermode coupling between IHB stretch and flanking group motions, we examined the possible fundamental vibrational modes in the  $800\text{--}1100\text{ cm}^{-1}$  region. A summary of the relevant frequencies and NM description can be found in [Table 2](#).

Table 1. Relative Energies (kJ mol<sup>-1</sup>) for (CH<sub>3</sub>OH)<sub>2</sub>H<sup>+</sup> at MP2 with Several Basis Sets<sup>a</sup>

| conformer | aug-cc-pVDZ       |                         |                    | 6-311++G(3df,3pd) |                         |                    | aug-cc-pVTZ       |                         |                    |
|-----------|-------------------|-------------------------|--------------------|-------------------|-------------------------|--------------------|-------------------|-------------------------|--------------------|
|           | electronic energy | electronic energy + ZPE | free energy (68 K) | electronic energy | electronic energy + ZPE | free energy (68 K) | electronic energy | electronic energy + ZPE | free energy (68 K) |
| MA        | 0.00              | 0.00                    | 0.00               | 0.00              | 0.00                    | 0.00               | 0.00              | 0.00                    | 0.00               |
| MB        | 2.04              | 1.86                    | 1.81               | 1.75              | 1.57                    | 1.53               | 1.91              | 1.68                    | 1.64               |

<sup>a</sup>Note: 1 Hartree = 2625.50 kJ mol<sup>-1</sup>. The number of basis functions for each basis set are as follows: aug-cc-pVDZ: 173, 6-311++G(3df,3pd): 318, and aug-cc-pVTZ: 391. Across all basis sets the most stable conformer is MA.

Table 2. MP2/aug-cc-pVDZ Harmonic Frequencies (cm<sup>-1</sup>) in the 800–1200 cm<sup>-1</sup> Region

| mode description                         | calculated frequencies |      |  |                    |
|--|------------------------|------|--|--------------------|
|  | conformer              |      | CH <sub>3</sub> OH <sub>2</sub> <sup>+</sup> | CH <sub>3</sub> OH |
|  | MA                     | MB   |  |                    |
| IHB/O–H <sup>+</sup> –O stretch          | 702                    | 691  |  |                    |
| CO stretch                               | 961                    | 954  | 822  | 1044               |
|  | 962                    | 990  |  |                    |
| COH deformation and CH <sub>3</sub> rock | 1026                   | 1040 |  |                    |
|  | 1092                   | 1068 | 941  | 1075               |
|  | 1172                   | 1171 | 1170   | 1169               |
|  | 1175                   | 1179 |  |                    |

In isolated CH<sub>3</sub>OH, there are three modes, namely, the C–O stretching mode (1044 cm<sup>-1</sup>) and two CH<sub>3</sub> rocking modes (1075 and 1169 cm<sup>-1</sup>).<sup>45</sup> Inspections of these rocking modes at MP2/aug-cc-pVDZ reveals that the lower frequency involves CH<sub>3</sub> rocking along the COH plane. Moreover, the said mode has a COH deformation and will be referred to as in-plane CH<sub>3</sub> rocking with COH deformation. The higher frequency mode, however, involves CH<sub>3</sub> rocking perpendicular to the COH plane (out-of-plane CH<sub>3</sub> rocking). Meanwhile, for CH<sub>3</sub>OH<sub>2</sub><sup>+</sup> harmonic frequencies of the above-mentioned modes are (1) C–O stretching ~822 cm<sup>-1</sup>, (2) in-plane CH<sub>3</sub> rocking ~941 cm<sup>-1</sup>, and (3) out-of-plane CH<sub>3</sub> rocking ~1170 cm<sup>-1</sup>. In (CH<sub>3</sub>OH)<sub>2</sub>H<sup>+</sup>, our calculations show six normal modes between 900 and 1200 cm<sup>-1</sup>. These modes correspond to in-phase and out-of-phase combinations from CH<sub>3</sub>OH and CH<sub>3</sub>OH<sub>2</sub><sup>+</sup> vibrations. The NM displacements and harmonic frequencies are compiled in Tables S3–S5 of the [Supporting Information](#). It was found that IHB motion is delocalized in out-of-phase C–O stretching and out-of-phase out-of-plane CH<sub>3</sub> rock. Also, significant COH deformation is found in modes involving CH<sub>3</sub> rock.

**Vibrational Hamiltonian.** Prior to vibrational treatments beyond harmonic approximation, a set of coordinates must be chosen for the Hamiltonian operator. Two commonly chosen coordinates are the local mode (LM) and traditional normal mode (NM) coordinates.<sup>46–48</sup> Usually, LM coordinates can describe the desired nuclear motion purer than NM coordinates. Such attributes of LM can be advantageous when the nuclear motion of interest is not neat in NM coordinates. Despite these disadvantages, setting up a Hamiltonian in NM coordinate is simpler. Using normal coordinates, the kinetic energy part is completely separable and all the anharmonicity and intermode coupling can be confined at the potential energy part. This is not always the case for LM coordinates, where the kinetic energies may not be separable and the coupling terms are partitioned in both kinetic and potential energy components.

In NM coordinates, the kinetic energies are separable and the vibrational Hamiltonian can be written as follows

$$H = \sum_{j=1}^n \frac{-\hbar^2}{2\mu_j} \frac{\partial^2}{\partial Q_j^2} + V(Q_1, Q_2, \dots, Q_j, \dots, Q_n) \quad (1)$$

where  $Q_j$  and  $\mu_j$  are the NM coordinate and effective mass for mode  $j$ , respectively, and  $V(Q_1, Q_2, \dots, Q_j, \dots, Q_n)$  is the potential energy surface (PES). The Hamiltonian above is under the approximation that vibrational angular momentum is negligible due to the large moment of inertia of (CH<sub>3</sub>OH)<sub>2</sub>H<sup>+</sup>. The numerical solution of the above differential equation can be achieved by means of standard finite difference methods (FDM).<sup>49</sup> However, for higher dimensional calculations, FDM would be very expensive. In particular, the cost of FDM would be  $\Pi g_i$ , where  $g_i$  is the number of grid points for the  $i$ th NM. As an example, if one would use 21 grid points for each degrees of freedom, then a four-dimensional FDM would require a total of  $21^4$  (194 481) single points. Such a requirement would discourage the use of large basis sets in evaluating single-point energies.

Alternatively, one can use a position-like basis to represent the Hamiltonian and is termed as discrete variable representation (DVR).<sup>35–38</sup> The main advantage of DVR is that it requires a smaller number of single-point evaluations, yet a large number of converged vibrational levels are obtained. Compared with our four-dimensional FDM case, a DVR calculation might only require  $7^4$  (2401) single-point evaluations. Such an advantage led us to adopt DVR with a harmonic oscillator as the basis function in this study. Interested readers can refer to the excellent detailed characterization of DVR by Light and co-workers.<sup>36,38</sup>

In all our DVR calculations the PES is calculated by a rigid scan along traditional NM coordinates (i.e., NM coordinates expanded as linear combinations of Cartesian displacements). The resulting Hamiltonian in DVR representation was diagonalize using the Davidson<sup>50</sup> algorithm. We used 7 DVR grids per degrees of freedom. Although a larger number of grid points would be more accurate, a comparison between 7 and 9 DVR grid points shows that the concerned calculated frequencies differs less than 2 cm<sup>-1</sup> (Table S6).

The electronic structure methods that we used for the PES construction are B3LYP, MP2, and CCSD(T). The performance of these methods was assessed by various combinations of basis sets. These include 6-31+G(d,p), 6-311+G(d,p), 6-311++G(3df,3pd), aug-cc-pVDZ, and aug-cc-pVTZ. Unfortunately, calculations at CCSD(T) with the two largest basis sets [6-311++G(3df,3pd) and aug-cc-pVTZ] are beyond our current computational resources and were not performed. For our CCSD(T)/basis set calculations, the reference geometry and NM corresponding to MP2/basis set were used to generate the PES. That is, we assumed that MP2 and CCSD(T) equilibrium geometries are in agreement with each other.

**Calculation of Integrated Absorption Coefficients.** To generate a predicted spectrum, the intensities must be calculated. We are aware that in “messenger-tagged” action

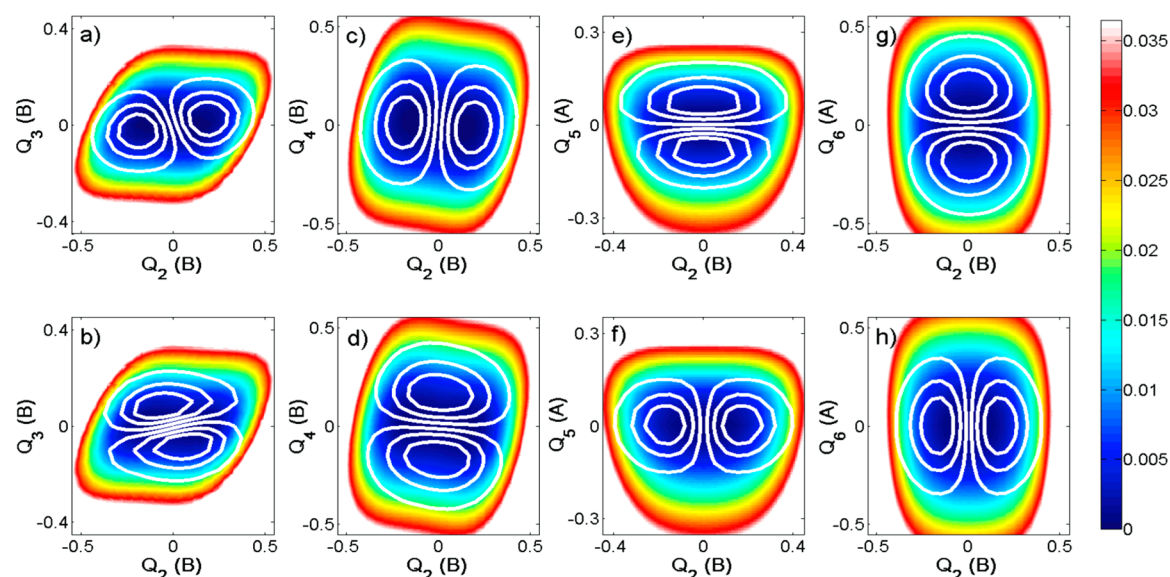


**Figure 3.** Two-dimensional (2D) wave functions obtained from the 2D potential cut at MP2/aug-cc-pVDZ for conformer MA. White contours refer to first and second excited state wave functions, and colored contours refer to the potential surface. The color bars are in Hartree units. It is evident that intermode coupling is due to the topology of the potential.  $Q_1$  refers to NM coordinate for O–O stretch,  $Q_2$  for IHB stretch,  $Q_3$  for out-of-phase C–O stretch,  $Q_4$  for out-of-phase in-plane  $\text{CH}_3$  rocking with COH deformation,  $Q_5$  in-phase C–O stretch, and  $Q_6$  in-phase in-plane  $\text{CH}_3$  rocking with COH deformation. The symmetry labels of these modes are placed on their respective axes labels. Only modes belonging to the same symmetry label for  $Q_2$  can couple with it.

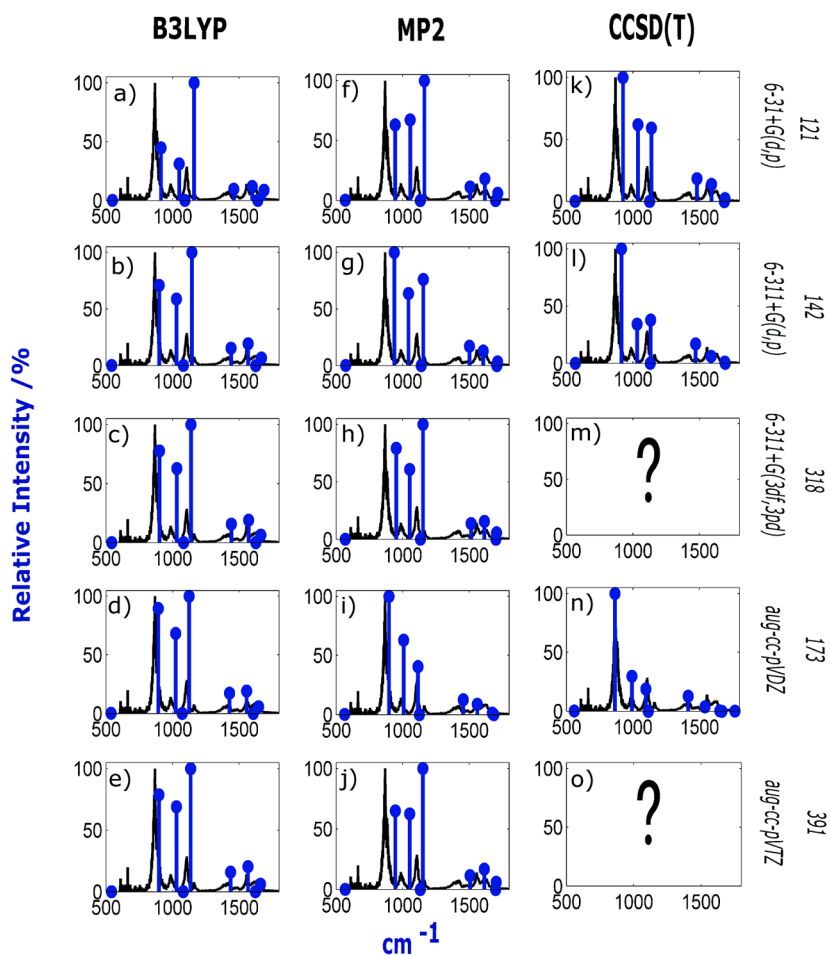


**Figure 4.** Four-dimensional (4D) DVR calculations for conformer MA at B3LYP, MP2, and CCSD(T) with several basis sets. The blue dots refer to the transition of the first few vibrational states relative to the ground vibrational state. The numbers on top of the basis set refers to the number of basis function.



**Table 3. Comparison of Harmonic and Anharmonic Frequencies (cm<sup>-1</sup>) for Conformer MA Revealing That Only Q<sub>2</sub> Is Significantly Anharmonic<sup>a</sup>**

| mode           | harmonic frequencies |        |                    |        | anharmonic frequencies |        |                      |        |
|----------------|----------------------|--------|--------------------|--------|------------------------|--------|----------------------|--------|
|                | MP2                  |        | B3LYP <sup>b</sup> |        | MP2                    |        | CCSD(T) <sup>c</sup> |        |
|                | cm <sup>-1</sup>     | km/mol | cm <sup>-1</sup>   | km/mol | cm <sup>-1</sup>       | km/mol | cm <sup>-1</sup>     | km/mol |
| Q <sub>1</sub> | 578                  | 2.4    | 575                | 2.3    | 578                    | 2.4    | 576                  | 2.7    |
| Q <sub>2</sub> | 702                  | 2502.8 | 1068               | 2222.9 | 1048                   | 2351.5 | 1010                 | 2566.8 |
| Q <sub>3</sub> | 961                  | 94.9   | 957                | 88.3   | 970                    | 94.3   | 969                  | 114.6  |
| Q <sub>4</sub> | 1092                 | 227.3  | 1100               | 224.9  | 1101                   | 226.7  | 1086                 | 247.7  |

<sup>a</sup>The anharmonic vibrational calculation was conducted using seven DVR grids at B3LYP, MP2, and CCSD(T) with aug-cc-pVDZ as basis. <sup>b</sup>The calculation was performed at B3LYP/aug-cc-pVDZ//MP2/aug-cc-pVDZ. <sup>c</sup>The calculation was performed at CCSD(T)/aug-cc-pVDZ//MP2/aug-cc-pVDZ.

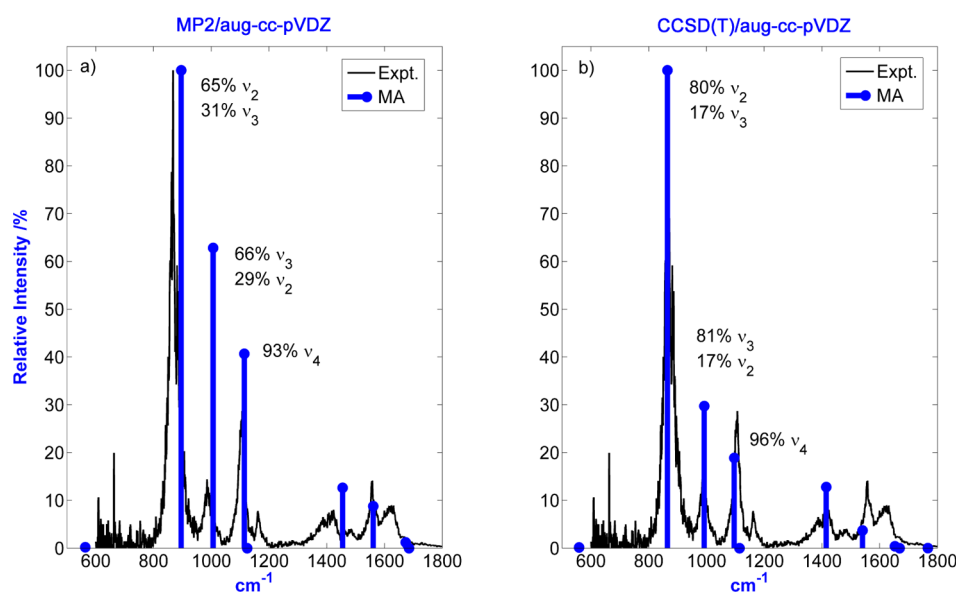


**Figure 5.** Four-dimensional calculation using (a) MP2/aug-cc-pVDZ and (b) CCSD(T)/aug-cc-pVDZ. In both figures, the blue dots refer to the transition of the first few vibrational states relative to the ground vibrational state. The mode labels are symmetric O–O stretching ( $\nu_1$ ), IHB stretching parallel to O–O axis ( $\nu_2$ ), out-of-phase C–O stretching ( $\nu_3$ ), and out-of-phase in-plane CH<sub>3</sub> rocking with COH deformation as ( $\nu_4$ ).

spectroscopy, the intensities are relative predissociation yields. Due to the complexity of simulating predissociation phenomenon, we instead calculate intensities in terms of integrated absorption coefficients and they are given by the expression below<sup>39</sup>

$$\mathcal{A}_{f0} = \left( \frac{\pi N_A}{3c\epsilon_0 \hbar} \right) \nu_{f0} |\langle \psi_0 | \hat{\mu} | \psi_f \rangle|^2$$

$$= 2.50664 \nu_{f0} |\langle \psi_0 | \hat{\mu} | \psi_f \rangle|^2 \text{ (in km mol}^{-1}\text{)} \quad (2)$$

where  $\hat{\mu}$  is the dipole moment operator in Debye,  $|\langle \psi_0 | \hat{\mu} | \psi_f \rangle|$  refers to the transition dipole moment, and  $\nu_{f0}$  is the  $\psi_0 \rightarrow \psi_f$  excitation energy in cm<sup>-1</sup>. Substitution of the physical constants results to the prefactor of 2.50664. The units of  $\mathcal{A}_{f0}$  are expressed in km mol<sup>-1</sup>. The dipole moment surfaces are calculated at the same levels with their corresponding PES, except for CCSD(T) where the dipole moment surfaces are obtained at CCSD level.

### 3. RESULTS AND DISCUSSION

**Intermode Coupling by Symmetry Considerations.** As mentioned earlier, the excess proton, H<sup>+</sup>, is located midpoint to the O–O axis. Moreover, it is evident from the Newman projections of MA and MB (Figure 1) that the only symmetry

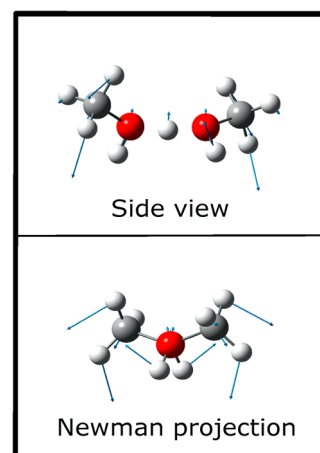


**Figure 6.** Normal mode that has a significant torsional character could possibly connect conformers MA and MB.

elements present are E and C<sub>2</sub>. Hence, both conformers belong to the C<sub>2</sub> point group. Referring to the corresponding character table, all of the normal modes can be categorized into A or B type symmetry.<sup>51</sup> To facilitate the discussion, we will first define the modes considered in the screening process. We are aware

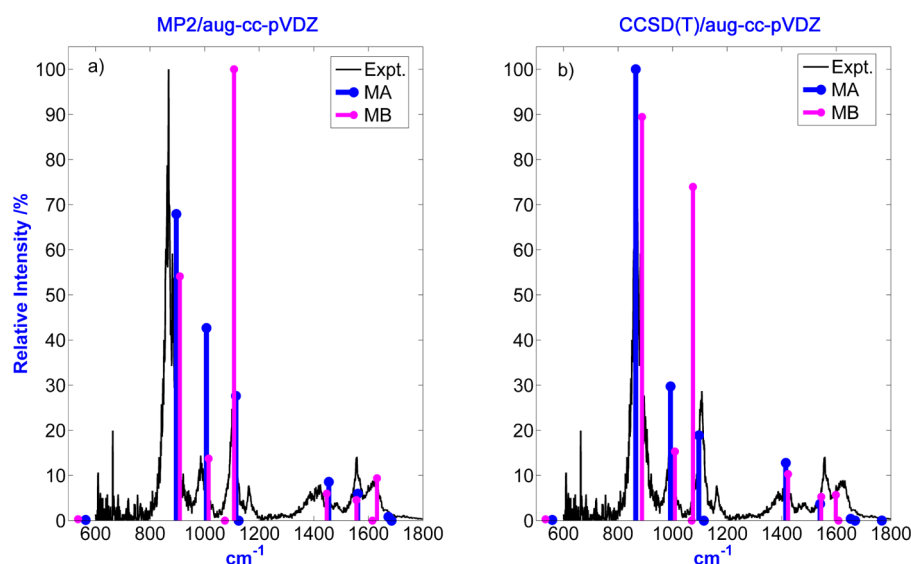


**Figure 7.** Comparison of the vibrational signatures of MA (blue) and MB (pink). The active role of torsional motion in modulating the coupling is evidenced by a distinct intensity distribution between MA and MB. However, the two conformers do not show any significant differences in their peak positions.

that these modes are difficult to describe and for simplicity we will call them as follows: (1) The low-frequency mode is the O–O stretch ( $\nu_1$ ), which on the basis of previous studies<sup>52</sup> exhibits a significant capability to modulate the IHB stretch frequency. (2) The IHB stretch is  $\nu_2$ . (3) Four modes are in the 800–1100  $\text{cm}^{-1}$  range, which include out-of-phase C–O stretch ( $\nu_3$ ), out-of-phase in-plane  $\text{CH}_3$  rocking with COH deformation ( $\nu_4$ ), in-phase C–O stretch ( $\nu_5$ ), and in-phase in-plane  $\text{CH}_3$  rocking with COH deformation ( $\nu_6$ ). In terms of symmetry classifications,  $\{\nu_2, \nu_3, \text{ and } \nu_4\}$  belong to type B symmetry whereas  $\{\nu_1, \nu_5, \text{ and } \nu_6\}$  are of type A symmetry.

To identify the possible modes that can couple with IHB, we performed a series of two-dimensional (2D) DVR (with IHB stretch) and three-dimensional (3D) DVR (with O–O and IHB stretches) calculations. These calculations were done at MP2/aug-cc-pVDZ. In 2D DVR calculations, both out-of-phase C–O stretch and out-of-phase in-plane  $\text{CH}_3$  rocking with COH deformation show a mixing with the IHB stretch. In 3D DVR calculations (Table S7 in Supporting Information), these two modes also show significant intensity enhancements. The 2D wave functions are compiled in Figure 3. It is evident that the fundamental bands in 800–1100  $\text{cm}^{-1}$  can couple with the IHB stretch provided that they belong to the same symmetry label (B). In the next section we will examine the intermode coupling between  $\nu_1$ ,  $\nu_2$ ,  $\nu_3$ , and  $\nu_4$  by running a four-dimensional (4D) DVR calculation using several quantum chemistry methods.

**Performance of Several Quantum Chemistry Methods.** Because the quality of a vibrational calculation would depend on the quality of the potential used to describe the nuclear motions, we assessed the performance of B3LYP, MP2, and CCSD(T) as a function of several basis sets. Because CCSD(T) does not have an analytical gradient, we have used the minima structures and normal mode displacements of their MP2 counterparts. The 4D DVR stick spectrum corresponding to MA at several theories and basis sets is presented in Figure 4. The experimental Ar-tagged action spectrum (black) measured and obtained from Johnson's<sup>4</sup> group is shown in the background for comparison.

For B3LYP calculations (Figure 4 left column), it is evident that among Pople basis sets (Figure 4a–c), the peak positions do not shift as the basis set is increased. However, significant redistributions on the intensities are observed with increasing basis sets. Comparison of the largest Pople basis set with aug-cc-pVDZ and aug-cc-pVTZ (Figure 4d,e) implies the convergence of intensities at large basis sets. Also, the most intense peak is favored to be around 1100  $\text{cm}^{-1}$ . Nevertheless, in terms of peak positions, a decent agreement with Johnson's<sup>4</sup> spectrum is observed.

Meanwhile, for MP2 calculations (Figure 4 middle column), the effect of the basis set's size is even more obvious. The most intense peak oscillates between  $\sim 950$  and  $\sim 1050$   $\text{cm}^{-1}$  across the Pople basis (Figure 4f–h). Turning our attention to Dunning basis, significant intensity redistribution is observed between aug-cc-pVDZ and aug-cc-pVTZ (Figure 4i,j). There is agreement between the calculated spectrum obtained from the largest Pople and aug-cc-pVTZ (Figure 4h,j). Also, it is surprising that aug-cc-pVDZ captured the peak positions of the experimental spectrum. It is also interesting to note that spectra obtained at 6-31+G(d,p) and aug-cc-pVTZ are pretty similar (Figure 4f,j).

Comparison between B3LYP and MP2 at aug-cc-pVDZ (Figure 4d,i) shows similar peak positions and differences only at their intensities. One might ask whether such discrepancy is due to the differences in normal modes or in the potential energy surface. To address this curiosity, vibrational calculation at the B3LYP level was performed using the equilibrium geometry and normal modes obtained at the MP2 level (i.e., B3LYP/aug-cc-pVDZ//MP2/aug-cc-pVDZ). We found that between MP2 and B3LYP PES, the latter favors intensity enhancements at higher frequencies. Comparison of a one-dimensional (1D) DVR for  $Q_2$  and  $Q_3$  at B3LYP/aug-cc-pVDZ//MP2/aug-cc-pVDZ and MP2/aug-cc-pVDZ//MP2/aug-cc-pVDZ (Table 3) shows that a slight shift ( $\leq 20$   $\text{cm}^{-1}$ ) can change the appearance of the spectrum. A similar trend was observed from the MP2 level vibrational calculation using the equilibrium structure and normal modes at the B3LYP level (i.e., MP2/aug-cc-pVDZ//B3LYP/aug-cc-pVDZ). From these findings, we determined that for a fixed basis set, the quality of

the potential surface can be more important than the differences in the normal modes obtained at various calculation levels. The 4D spectra for calculations at B3LYP/aug-cc-pVDZ//MP2/aug-cc-pVDZ and vice versa can be found in the [Supporting Information](#) (Figures S5–S6).

Lastly, in the right column in [Figure 4](#) are vibrational calculations at the CCSD(T) level using the equilibrium geometries and normal modes of their MP2 counterparts (i.e., CCSD(T)/basis//MP2/basis). Due to the intensive memory requirements of a CCSD(T) job and limitations in computational resources, we only conducted our CCSD(T) calculation at 6-31+G(d,p), 6-311+G(d,p), and aug-cc-pVDZ bases. By comparison of MP2 and CCSD(T) vibrational calculations ([Figure 4](#) middle and right columns), it is evident that across the basis sets, CCSD(T) favors the most intense peak at lower frequencies. Furthermore, MP2 and CCSD(T) calculations ([Figure 4i,n](#)) at aug-cc-pVDZ show excellent agreement with the experimental spectrum.

Despite this agreement at the smallest Dunning basis set, it would be worthwhile to explore basis sets larger than aug-cc-pVDZ. As shown in [Figure 4i,j](#), moving from aug-cc-pVDZ to aug-cc-pVTZ at the MP2 level, the most intense peak was favored at higher frequencies. As mentioned earlier, the spectrum obtained at 6-31+G(d,p) and aug-cc-pVTZ are almost similar. Whether this comparison is fortuitous or not can only be answered by a calculation at even larger basis sets. One of these basis sets might be aug-cc-pVQZ, which has 734 basis functions for our system. Although we desire to achieve convergence with the size of the basis sets, we are limited by our current computational hardware. Hence, we declare that we have not reached quantum chemical convergence in our calculations. Despite this issue, all of the 13 4D DVR calculations in [Figure 4](#) have captured the existence of intermode coupling. From these quantum chemistry methods, we will focus our discussions on the highest level that we can afford, which is CCSD(T)/aug-cc-pVDZ. Whenever applicable, a brief discussion for MP2/aug-cc-pVDZ will be made.

**Among the Four Modes, Only IHB Is Strongly Anharmonic.** To further understand the 4D DVR spectrum shown in [Figure 4](#), a one-dimensional (1D) cut was taken from the 4D PES and were used to estimate the anharmonically corrected vibrational frequencies. This was done by performing a 1D DVR calculation. The harmonic as well as anharmonically corrected frequencies are summarized in [Table 3](#). A comparison between harmonic and anharmonic frequencies reveals that among the modes, only  $Q_2$  is significantly anharmonic, as noted by a large shift ( $>300\text{ cm}^{-1}$ ) across all methods. A closer look at the 1D PES reveals the dominance of higher order terms in the potential energy curve ([Figure S7](#)).

**Quantum Picture of Intermode Coupling.** If one would revisit  $\text{H}_5\text{O}_2^+$ , the IHB stretch couples with a combination band between two low-frequency modes: O–O stretching and water wagging.<sup>25,30</sup> However, we found a different scenario for  $(\text{CH}_3\text{OH})_2\text{H}^+$ , where two fundamental modes of moderate frequency couples directly with the IHB stretch. Such distinct coupling between  $\text{H}_5\text{O}_2^+$  and  $(\text{CH}_3\text{OH})_2\text{H}^+$  highlights the active role of flanking group motions near the vicinity of IHB stretching frequency.

A magnified version of the stick spectrum for MP2 and CCSD(T) with aug-cc-pVDZ is shown in [Figure 5](#). One notable feature is the decent agreement with experimental data on the positions of three main peaks at  $800\text{--}1200\text{ cm}^{-1}$ . At this point, agreements on peak positions rather than intensities are

better comparisons due to the predissociation nature of the experimental spectrum. Furthermore, the calculated intensities correspond to absorption, whereas experimental intensities are predissociation yields. The most intense band along  $880\text{ cm}^{-1}$  was successfully recovered in the calculation. Relative intensities among two calculated peaks around  $1000$  and  $1100\text{ cm}^{-1}$  did not fully capture the experimental features. An additional weak peak at  $1160\text{ cm}^{-1}$  seen in experimental measurement is probably a combination band that was not accounted for in the calculation. Alternatively, it could have also been due to the differences in symmetry between  $(\text{CH}_3\text{OH})_2\text{H}^+$  and  $\text{Ar}\cdot(\text{CH}_3\text{OH})_2\text{H}^+$ . In our calculations, combination bands between  $\nu_1$  and  $\nu_2\text{--}\nu_4$  are located between  $1400$  and  $1700\text{ cm}^{-1}$ . Due to the existence of other fundamental modes, which are excluded in the four-dimensional calculation, an attempt for assignment was not made. Some of these modes include  $\text{H}^+$  and free O–H bending.

Due to such intermode coupling, a definite assignment is not possible. Instead, we express the resulting wave functions as a linear combination of the independent wave functions for  $\nu_1\text{--}\nu_4$ . To understand the extent of mixing, a set of test states are constructed by taking the direct products of the anharmonically corrected one-dimensional wave functions for  $\nu_1\text{--}\nu_4$ . The four-dimensional wave functions were projected onto the resulting test states, yielding its linear combination coefficient. The percentages shown in [Figure 5a,b](#) are the squares of the linear combination coefficients, which in turn are mode contributions for a particular peak. Note that percentages due to combination bands:  $\nu_1 + \nu_2$ ,  $\nu_1 + \nu_3$ , and  $\nu_1 + \nu_4$  are counted as  $\nu_2$ ,  $\nu_3$ , and  $\nu_4$  respectively. Also, the discrepancies of the percentage sum from 100% for each peak are due to other states that are less than 2% in contribution.

**Comments on the Role of Torsional Motion.** Between the two conformers in [Figure 1](#), it is expected from energy considerations that MA will be more expressed in the spectrum than MB. To quantify how much MA is expressed over MB, we calculated the relative populations of MA and MB using

$$\Delta G = -RT \ln \left( \frac{y_{\text{MB}}}{100 - y_{\text{MB}}} \right) \quad (3)$$

where  $100 - y_{\text{MB}}$  and  $y_{\text{MB}}$  are the population percentage of MA and MB, respectively,  $R$  is the molar gas constant, and  $T$  is the cluster's temperature in Kelvin. Although the exact temperatures of MA and MB are not known at experimental conditions, we will adopt a value of 68 K, which Iyengar<sup>53</sup> reported in his AIMD simulation. Across all the free energies in [Table 1](#), the MA population is greater than 94%, implying that MA spectrum greatly contributes on the overall experimental spectrum.

To evaluate the effect of HOOH torsional motion ([Figure 6](#)) on the spectrum, a similar four-dimensional calculation was performed on conformer MB. Calculated spectra for both MA and MB conformers are compiled in [Figure 7](#). Despite the unnoticeable shift in peak positions, it is evident that relative intensities are sensitive to HOOH torsional motion. Such distinct intensity distributions between MA and MB suggest the active role of torsional motion.

## 4. CONCLUSIONS

In summary, we have confirmed that flanking group motions can couple with IHB motion in *Zundel*  $(\text{CH}_3\text{OH})_2\text{H}^+$ . Such a new form of coupling with O–O stretching, out-of-phase C–O



stretching, and out-of-phase in-plane  $\text{CH}_3$  rocking with COH deformation are reported.  $\text{H}_5\text{O}_2^+$  reveals the role of combination tones arising from low-frequency modes, but our studies for  $(\text{CH}_3\text{OH})_2\text{H}^+$  unveil a distinct form of coupling between fundamental bands of the flanking group motions.

## ■ ASSOCIATED CONTENT

### Supporting Information

The Supporting Information is available free of charge on the ACS Publications website at DOI: 10.1021/acs.jpca.5b10554.

Optimized structures; 2D wavefunctions; vibrational calculations and IR spectra; screening of flanking groups; potential energy curve; harmonic frequencies and normal mode displacement vectors for  $(\text{MeOH})_2\text{H}^+$ ; selection of normal modes; table of frequencies and intensities from the four-dimensional calculations using MP2 and CCSD-(T); table of projections of the direct products (PDF)

## ■ AUTHOR INFORMATION

### Corresponding Author

\*Jer-Lai Kuo. E-mail: jlkuo@pub.iams.sinica.edu.tw.

### Present Address

<sup>||</sup>Institute of Atomic and Molecular Sciences, Academia Sinica, No. 1 Roosevelt Road, Section 4, Taipei 10617, Taiwan.

### Notes

The authors declare no competing financial interest.

## ■ ACKNOWLEDGMENTS

This work was financially supported by various grants from Academia Sinica and the Ministry of Science and Technology (MOST) of Taiwan under MOST101-2113-M-001-023-MY3 and MOST104-2113-M-001-017. J.A.T. thanks the Taiwan International Graduate Program (TIGP) for scholarship and MOST for travel support. Computational resources are supported in part by the National Center for High Performance Computing (NCHC). We thank Prof. Yonggang Yang and Dr. Kaito Takahashi for the fruitful discussions related to this project. We express our gratitude to Jheng-Wei Li for the DVR scanner and Dr. Masato Morita for the DVR solver. We are also grateful to Prof. Mark A. Johnson for providing the experimental Ar-tagged action spectrum.

## ■ REFERENCES

- (1) Tuckerman, M. E.; Marx, D.; Klein, M. L.; Parrinello, M. On the Quantum Nature of the Shared Proton in Hydrogen Bonds. *Science* **1997**, *275*, 817–820.
- (2) Gerlt, J. A.; Kreevoy, M. M.; Cleland, W.; Frey, P. A. Understanding enzymic catalysis: the importance of short, strong hydrogen bonds. *Chem. Biol.* **1997**, *4*, 259–267.
- (3) Meot-Ner, M. The ionic hydrogen bond. *Chem. Rev.* **2005**, *105*, 213–284.
- (4) Roscioli, J. R.; McCunn, L. R.; Johnson, M. A. Quantum structure of the intermolecular proton bond. *Science* **2007**, *316*, 249–254.
- (5) Olesen, S. G.; Guasco, T. L.; Roscioli, J. R.; Johnson, M. A. Tuning the intermolecular proton bond in the  $\text{H}_5\text{O}_2^+$  'Zundel ion' scaffold. *Chem. Phys. Lett.* **2011**, *509*, 89–95.
- (6) Graham, J. D.; Buytendyk, A. M.; Wang, D.; Bowen, K. H.; Collins, K. D. Strong, low-barrier hydrogen bonds may be available to enzymes. *Biochemistry* **2014**, *53*, 344–349.
- (7) Asmis, K. R.; Pivonka, N. L.; Santambrogio, G.; Brümmer, M.; Kaposta, C.; Neumark, D. M.; Wöste, L. Gas-phase infrared spectrum of the protonated water dimer. *Science* **2003**, *299*, 1375–1377.

- (8) Fridgen, T. D.; MacAleese, L.; Maitre, P.; McMahon, T. B.; Boissel, P.; Lemaire, J. Infrared spectra of homogeneous and heterogeneous proton-bound dimers in the gas phase. *Phys. Chem. Chem. Phys.* **2005**, *7*, 2747–2755.

- (9) Fridgen, T. D.; Macaleese, L.; McMahon, T. B.; Lemaire, J.; Maitre, P. Gas phase infrared multiple-photon dissociation spectra of methanol, ethanol and propanol proton-bound dimers, protonated propanol and the propanol/water proton-bound dimer. *Phys. Chem. Chem. Phys.* **2006**, *8*, 955–966.

- (10) Fridgen, T. D.; McMahon, T. B.; MacAleese, L.; Lemaire, J.; Maitre, P. Infrared Spectrum of the Protonated Water Dimer in the Gas Phase. *J. Phys. Chem. A* **2004**, *108*, 9008–9010.

- (11) Ricks, A. M.; Doublerly, G. E.; Duncan, M. A. Infrared spectroscopy of the protonated nitrogen dimer: The complexity of shared proton vibrations. *J. Chem. Phys.* **2009**, *131*, 104312.

- (12) Headrick, J. M.; Diken, E. G.; Walters, R. S.; Hammer, N. I.; Christie, R. A.; Cui, J.; Myshakin, E. M.; Duncan, M. A.; Johnson, M. A.; Jordan, K. D. Spectral signatures of hydrated proton vibrations in water clusters. *Science* **2005**, *308*, 1765–1769.

- (13) McCunn, L. R.; Roscioli, J. R.; Johnson, M. A.; McCoy, A. B. An H/D isotopic substitution study of the  $\text{H}_5\text{O}_2^+$ . Ar vibrational predissociation spectra: exploring the putative role of Fermi resonances in the bridging proton fundamentals. *J. Phys. Chem. B* **2008**, *112*, 321–327.

- (14) Hammer, N. I.; Diken, E. G.; Roscioli, J. R.; Johnson, M. A.; Myshakin, E. M.; Jordan, K. D.; McCoy, A. B.; Huang, X.; Bowman, J. M.; Carter, S. The vibrational predissociation spectra of the  $\text{H}_5\text{O}_2^+$  +  $\text{RGn}$  ( $\text{RG} = \text{Ar, Ne}$ ) clusters: correlation of the solvent perturbations in the free OH and shared proton transitions of the Zundel ion. *J. Chem. Phys.* **2005**, *122*, 244301.

- (15) Moore, D. T.; Oomens, J.; van der Meer, L.; von Helden, G.; Meijer, G.; Valle, J.; Marshall, A. G.; Eyler, J. R. Probing the vibrations of shared, OH+O-bound protons in the gas phase. *ChemPhysChem* **2004**, *5*, 740–743.

- (16) Jiang, J.; Wang, Y.; Chang, H.; Lin, S. H.; Lee, Y. T.; January, R. V. *J. Am. Chem. Soc.* **2000**, *122*, 1398–1410.

- (17) Yeh, L. I.; Okumura, M.; Myers, J. D.; Price, J. M.; Lee, Y. T. Vibrational spectroscopy of the hydrated hydronium cluster ions  $\text{H}_3\text{O}^+(\text{H}_2\text{O})_n$  ( $n = 1, 2, 3$ ). *J. Chem. Phys.* **1989**, *91*, 7319–7330.

- (18) Okumura, M.; Yeh, L. I.; Lee, Y. T. Infrared spectroscopy of the cluster ions  $\text{H}+3(\text{H}_2)_n$ . *J. Chem. Phys.* **1988**, *88*, 79.

- (19) Diken, E. G.; Headrick, J. M.; Roscioli, J. R.; Bopp, J. C.; Johnson, M. A.; McCoy, A. B. Fundamental excitations of the shared proton in the  $\text{H}_3\text{O}_2^-$  and  $\text{H}_5\text{O}_2^+$  complexes. *J. Phys. Chem. A* **2005**, *109*, 1487–1490.

- (20) Lee, H. M.; Kumar, A.; Kolaski, M.; Kim, D. Y.; Lee, E. C.; Min, S. K.; Park, M.; Choi, Y. C.; Kim, K. S. Comparison of cationic, anionic and neutral hydrogen bonded dimers. *Phys. Chem. Chem. Phys.* **2010**, *12*, 6278–6287.

- (21) McCoy, A. B.; Huang, X.; Carter, S.; Landeweer, M. Y.; Bowman, J. M. Full-dimensional vibrational calculations for  $\text{H}_5\text{O}_2^+$  using an ab initio potential energy surface. *J. Chem. Phys.* **2005**, *122*, 061101.

- (22) Valeev, E. F.; Schaefer, H. F. The protonated water dimer: Brueckner methods remove the spurious  $\text{C}_1$  symmetry minimum. *J. Chem. Phys.* **1998**, *108*, 7197.

- (23) Xie, Y.; Remington, R. B.; Schaefer, H. F. The protonated water dimer: Extensive theoretical studies of  $\text{H}_5\text{O}_2^+$ . *J. Chem. Phys.* **1994**, *101*, 4878–4884.

- (24) Vendrell, O.; Gatti, F.; Lauvergnat, D.; Meyer, H.-D. Full-dimensional (15-dimensional) quantum-dynamical simulation of the protonated water dimer. I. Hamiltonian setup and analysis of the ground vibrational state. *J. Chem. Phys.* **2007**, *127*, 184302.

- (25) Vendrell, O.; Gatti, F.; Meyer, H.-D. Full dimensional (15-dimensional) quantum-dynamical simulation of the protonated water dimer. II. Infrared spectrum and vibrational dynamics. *J. Chem. Phys.* **2007**, *127*, 184303.

- (26) Vendrell, O.; Brill, M.; Gatti, F.; Lauvergnat, D.; Meyer, H.-D. Full dimensional (15-dimensional) quantum-dynamical simulation of



the protonated water-dimer III: Mixed Jacobi-valence parametrization and benchmark results for the zero point energy, vibrationally excited states, and infrared spectrum. *J. Chem. Phys.* **2009**, *130*, 234305.

(27) Vendrell, O.; Gatti, F.; Meyer, H.-D. Full dimensional (15 dimensional) quantum-dynamical simulation of the protonated water-dimer IV: isotope effects in the infrared spectra of  $D(D_2O)_2^+$ ,  $H(D_2O)_2^+$ , and  $D(H_2O)_2^+$  isotopologues. *J. Chem. Phys.* **2009**, *131*, 034308.

(28) Vener, M. V.; Kühn, O.; Sauer, J. The infrared spectrum of the  $O\cdots H\cdots O$  fragment of  $H_5O_2^+$ : Ab initio classical molecular dynamics and quantum 4D model calculations. *J. Chem. Phys.* **2001**, *114* (1), 240.

(29) Huang, X.; Braams, B. J.; Bowman, J. M. Ab initio potential energy and dipole moment surfaces for  $H_5O_2^+$ . *J. Chem. Phys.* **2005**, *122*, 044308.

(30) Vendrell, O.; Gatti, F.; Meyer, H. D. Dynamics and infrared spectroscopy of the protonated water dimer. *Angew. Chem., Int. Ed.* **2007**, *46* (36), 6918–6921.

(31) Cheng, H.-P.; Krause, J. L. The dynamics of proton transfer in  $H_5O_2^+$ . *J. Chem. Phys.* **1997**, *107* (20), 8461.

(32) Sauer, J.; Döbler, J. Gas-Phase Infrared Spectrum of the Protonated Water Dimer: Molecular Dynamics Simulation and Accuracy of the Potential Energy Surface. *ChemPhysChem* **2005**, *6* (9), 1706–1710.

(33) Sobolewski, A. L.; Domcke, W. Ab Initio Investigation of the Structure and Spectroscopy of Hydronium–Water Clusters. *J. Phys. Chem. A* **2002**, *106*, 4158–4167.

(34) Möller, C.; Plesset, M. S. Note on an approximation treatment for many-electron systems. *Phys. Rev.* **1934**, *46*, 618–622.

(35) Colbert, D. T.; Miller, W. H. A novel discrete variable representation for quantum mechanical reactive scattering via the S-matrix Kohn method. *J. Chem. Phys.* **1992**, *96*, 1982.

(36) Light, J. C.; Hamilton, I. P.; Lill, J. V. Generalized discrete variable approximation in quantum mechanics. *J. Chem. Phys.* **1985**, *82*, 1400.

(37) Bacic, Z.; Light, J. C. Theoretical Methods For Rovibrational States Of Floppy Molecules. *Annu. Rev. Phys. Chem.* **1989**, *40*, 469–498.

(38) Light, J. C.; Carrington, T. Discrete Variable Representations and their Utilization. In *Advances in Chemistry and Physics*; Prigogine, I., Rice, S. A., Eds.; John Wiley and Sons: New York, 2000; Chapter 4.

(39) Atkins, P. W.; Friedman, R. S. *Molecular Quantum Mechanics*, 4th ed.; Oxford University Press: New York, 2005; pp 538–541.

(40) Bartlett, R. J.; Purvis, G. D., III. Many-body perturbation-theory, coupled-pair many-electron theory, and importance of quadruple excitations for correlation problem. *Int. J. Quantum Chem.* **1978**, *14*, 561–81.

(41) Pople, J. A.; Krishnan, R.; Schlegel, H. B.; Binkley, J. S. Electron Correlation Theories and Their Application to the Study of Simple Reaction Potential Surfaces. *Int. J. Quantum Chem.* **1978**, *14*, 545–60.

(42) Becke, A. D. Density-functional thermochemistry. III. The role of exact exchange. *J. Chem. Phys.* **1993**, *98*, 5648–52.

(43) Frisch, M. J.; Trucks, G. W.; Schlegel, H. B.; et al. *Gaussian 09*, Revision D.01; Gaussian, Inc.: Wallingford, CT, 2009.

(44) Marx, D. Proton transfer 200 years after von Grotthuss: insights from ab initio simulations. *ChemPhysChem* **2006**, *7*, 1848–1870.

(45) Shimanouchi, T. *Tables of Molecular Vibrational Frequencies Consolidated Vol. I*; National Bureau of Standards: Washington, DC, 1972.

(46) Ogata, Y.; Kawashima, Y.; Takahashi, K.; Tachikawa, M. Theoretical vibrational spectra of  $OH^-(H_2O)_2$ : the effect of quantum distribution and vibrational coupling. *Phys. Chem. Chem. Phys.* **2015**, *17*, 25505–25515.

(47) Morita, M.; Takahashi, K. Multidimensional local mode calculations for the vibrational spectra of  $OH^-(H_2O)_2$  and  $OH^-(H_2O)_2\cdots Ar$ . *Phys. Chem. Chem. Phys.* **2013**, *15* (36), 14973.

(48) McCoy, A. B. The role of electrical anharmonicity in the association band in the water spectrum. *J. Phys. Chem. B* **2014**, *118* (28), 8286–8294.

(49) Epperson, J. F. *An Introduction to Numerical Methods and Analysis*; John Wiley and Sons Inc.: New York, 2002; p 518.

(50) Stathopoulos, A.; Fischer, C. F. A Davidson program for finding a few selected extreme eigenpairs of a large, sparse, real, symmetric matrix. *Comput. Phys. Commun.* **1994**, *79* (2), 268–290.

(51) Graybeal, J. D. *Molecular Spectroscopy*; McGraw-Hill: Singapore, 1988; pp 501–506.

(52) Tan, J. A.; Li, J.-W.; Kuo, J.-L. Proton Quantum Confinement on Symmetric Dimers of Ammonia and Lower Amine Homologs. In *Frontiers in Quantum Methods and Applications in Chemistry and Physics Selected Proceedings of QSCP-XVIII (Paraty, Brazil, December, 2013)*; Nascimento, M. A., Maruani, J., Brandas, E. J., Delgado-Barrio, G., Eds.; Springer: Berlin, 2015; pp 77–89.

(53) Li, X.; Moore, D. T.; Iyengar, S. S. Insights from first principles molecular dynamics studies toward infrared multiple-photon and single-photon action spectroscopy: Case study of the proton-bound dimethyl ether dimer. *J. Chem. Phys.* **2008**, *128*, 184308.